

Efficient Volume Reduction of Optimally Designed Pyramidal Log-Periodic Antennas via Meander Elements

Stamatios A. Amanatiadis, Antonios X. Lalas, Nikolaos V. Kantartzis, and Theodoros D. Tsiboukis

Department of Electrical and Computer Engineering
Aristotle University of Thessaloniki, Thessaloniki GR-54124, Greece
samanati@auth.gr, lant@faraday.ee.auth.gr, kant@auth.gr and tsiboukis@auth.gr

Abstract — A class of volume-optimized pyramidal log-periodic antennas (PLPAs) with an adjustable ultra wideband performance is introduced in this paper. To this aim, a parametric analysis is initially conducted to decrease the total size of the prototype Euclidean-toothed PLPA. The new structures are based on the concept of meander curves, which leads to efficient substitutes of the conventional device with drastically reduced dimensions, but equivalent behavior. For the design procedure, the radiation features of all antennas are accurately evaluated via a 3-D finite-difference time-domain (FDTD) algorithm. Extensive investigation reveals that the prior volume-confinement method and the proposed radiators can provide very compact setups for a variety of modern communication systems.

Index Terms — FDTD methods, log-periodic antennas, pyramidal antennas, and volume optimization.

I. INTRODUCTION

Log-periodic antennas (LPAs) exhibit a notable frequency-independent behavior with a relatively sensible size, so constituting an ideal choice for broadband applications. A mainstream and easily fabricated kind is the planar LPA that combines the majority of wideband antenna benefits with the functional attributes of planar topologies [1-6]. However, since the 3-dB main lobe contour of the particular radiator is elliptical, its use as a feeder for parabolic reflectors is rather prohibitive. Fortunately, this defect can be overcome by a two-arm non-planar LPA configuration, in which the inclination angle of its two arms equals the corresponding single arm opening angle [7]. In this manner, a

unidirectional beam with a circular 3-dB contour, that maximizes the directivity of the reflector, is obtained. Also, the main lobe polarization is quasi-linear, thus leading to a dual polarization property in the case of a pyramidal structure formed by two such vertically polarized antennas. Operating independently, these radiators are proven fairly profitable, since they attain a double bandwidth, when employed for the same application or, alternatively, as distinct transmission and reception [8].

Therefore, it becomes apparent that pyramidal log-periodic antennas (PLPAs) can be used in ultra wideband (UWB) systems, which is optimum for substantial directivity like space-based radars [9-13] and specialized microwave remote sensing arrangements [14-18]. These structures nonetheless should have a very limited overall size; a critical necessity that can be hardly satisfied by traditional PLPAs. Hence, it is the purpose of this paper to present a novel family of volume-controllable PLPAs with confined dimensions and advanced radiation characteristics. The design process starts with a PLPA of Euclidean elements, whose size is consistently minimized to allow cost-effective solutions in diverse realizations. In this context, a comprehensive parametric study is conducted for the optimization of the appropriate antenna traits in terms of compactness. Essentially, the key asset of the proposed PLPA class lies on the systematic incorporation of meander elements whose unique geometry achieves significant volume reductions without affecting the devices' desired performance. The radiators so developed, apart from being fabricated, are precisely analyzed via a 3-D finite-difference time-domain (FDTD) method. Results indicate the efficiency of the volume-reduction

method and confirm the advantages of the proposed antennas.

II. SYSTEMATIC DESIGN OF COMPACT UWB PLPAs

A. Theory and geometric description

A practical antenna geometry, which can sufficiently support a frequency-independent behavior is specified by two or more angles, a scale factor, and two finite segments. Fulfilling these design criteria, the PLPA with Euclidean elements exhibits a broadband performance. The pattern of a single arm, as depicted in Fig. 1, is formed via similarly-shaped rectangles of thickness t_n , attached in electric contact to a central conductor (“boom”) with adjacent element dimensions differing by a constant scale factor $\tau < 1$. In particular, linear segments l_{\max} and l_{\min} determine the minimum and maximum operating frequency of the structure, respectively. Note that two opposite elements, in the same arm, act like $\lambda/2$ dipoles; thus l_{\max} should be $\lambda_{\min}/4$ long, for λ_{\min} the wavelength corresponding to the minimum desired operating frequency. However, these valuable properties can be acquired only when more than one elements are tuned, and therefore the dimension of the largest tooth has to be increased by about 70 %. Likewise, the smallest element in the arm must be $\lambda_{\max}/4$ long, with λ_{\max} the wavelength associated to the maximum desired frequency, while, owing to the aforementioned reason, its dimension needs to be decreased by almost 75 %.

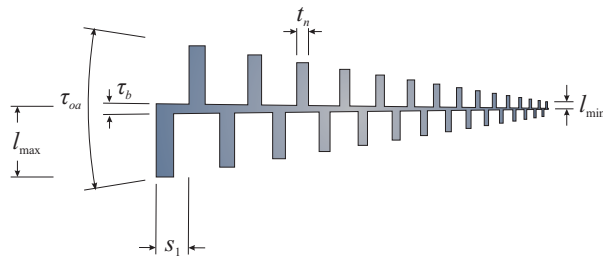


Fig. 1. Geometry of a Euclidean-toothed arm.

On the other hand, τ_{oa} and τ_b indicate the opening angles of the arm and the central boom, respectively, whereas τ_a (Fig. 2 (a)) denotes the inclination angle between two opposite arms. Based on these variables the remaining geometrical details of the single arm can be readily obtained. Specifically, the length of the antenna arm is given by,

$$L = (l_{\max} - l_{\min}) \cot(\tau_{oa} / 2) \quad (1)$$

with its teeth number calculated in terms of

$$N = 1 + \frac{\log(l_{\min} / l_{\max})}{\log \tau}, \quad (2)$$

on condition that $l_{\min} = l_{\max} \tau^{N-1}$ and N is an integer. Then, the distance s_n between two consecutive elements (designating as s_1 its largest possible value) is computed via the recursive formula of,

$$s_n = s_{n-1} \tau = s_1 \tau^{n-1}, \quad \text{for } s_1 = \frac{l_{\max} (1 - \tau^{N-1})}{\tan(\tau_{oa} / 2)} \frac{1 - \tau}{1 - \tau^N} \quad (3)$$

taking into account that

$$L = \sum_{n=1}^N s_1 \tau^{n-1} = s_1 \frac{1 - \tau^N}{1 - \tau}. \quad (4)$$

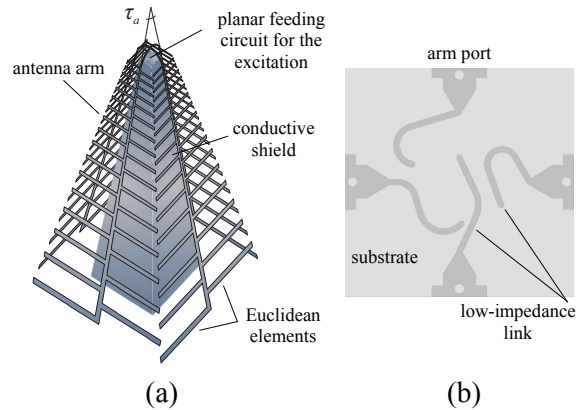


Fig. 2. The four-arm PLPA with Euclidean elements and a pyramidal grounded conductive shield for (a) perspective view and (b) planar feeding circuit.

Consistent with the previous geometric analysis, the proposed four-arm PLPA is illustrated in Fig. 2 (a). In its hollow pyramidal-shaped interior, we place a grounded highly conductive shield to create an effectively screened from internal electromagnetic fields storage space, which can conveniently accommodate the feeding electronics of the antenna close to its terminals. The typical shape of the shield is square pyramidal with an opening angle of about half the τ_a value [8]; a selection which improves the gain of the radiator and considerably maintains its frequency independence. It is stressed that τ_a should be equal to τ_{oa} in order to accomplish a circular 3-dB main lobe contour. Moreover, the entire device is fed by a properly developed planar circuit (Fig. 2 (b)), located on the narrow apex of the pyramidal shield, whose main goal is to guaran-

tee constant low-impedance links between the arms of the PLPA and its electronics. In this way, the radiation modes of the antenna are not disrupted, while the common need for long transmission line cables (and their undesired inevitable losses) is avoided. Finally, our radiator is designed to operate in the broad range of nearly 20 GHz to 80 GHz. This indicates that the electrical lengths of its largest and smallest elements are chosen (and kept fixed throughout this paper) to be 6.35 mm and 0.41 mm, respectively. Observe that for the case of Euclidean teeth, these values are equal to l_{\max} and l_{\min} .

B. Computational implementation aspects

The radiating characteristics of the antennas, under study, are obtained in terms of a 3-D FDTD method. Its spatial increments, which specify the appropriate cell size, are set to $\Delta x = \Delta y = 0.039$ mm and $\Delta z = 0.102$ mm, while the corresponding time-step is $\Delta t = 27.65$ fs, according to the Courant stability condition. The computational space is excited via the bandpass Gaussian pulse

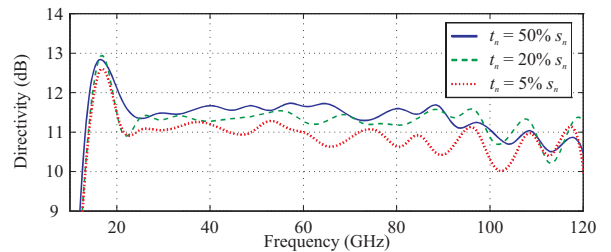
$$f(t) = e^{-(t/t_p - 6)^2/2} \sin(2\pi f_0 t), \quad (5)$$

placed at the planar feeding circuit of Fig. 2. To attain our antenna's operational range, the waveform parameters of the excitation are selected as $t_p = 5.55$ ps and $f_0 = 62.5$ GHz, thus producing an ample spectrum from 5 GHz to 120 GHz. In this way, the very satisfactory grid resolution of approximately $\lambda/55$ (λ the smallest wavelength of the simulation) is accomplished. Open boundaries are terminated by a perfectly matched layer (PML) [19-22] with an air buffer of 0.6λ from the radiator. The PML is $\delta = 8$ layers (cells) thick, while for its attenuation parameters: (a) the loss grading σ (similarly σ^*) is set to be quadratic ($n = 2$), i.e., $\sigma(\rho) = \sigma_{\max}(\rho/\delta)^n$ ($\rho = x, y, z$) and (b) the reflection factor $R = \exp\{-2\sigma_{\max}\delta/(n+1)\epsilon_0 c\}$ is set to $R = 10^{-6}$, with c the vacuum speed of light. In particular, (σ, σ^*) vary quadratically along the ρ direction from 0 at each vacuum-PML interface to the peak values of ($\sigma_{\max} = 1.23 \times 10^5$ S/m, $\sigma_{\max}^* = 1.64 \times 10^{10}$ Ω /m), allowing trivial reflections only below -80 dB across the entire source spectrum. It is stressed that the above numerical setup remains the same for every example in the paper. Hence, we are able to certify the profits of our volume reduction method by modifying only the size of the lattice. Lastly, all simulations are conducted on a 3.47 GHz IntelTM

Xeon dual-processor X5690 computer with 96 GB RAM for a total number of 82.678 time-steps.

C. Numerical results and measurements

Recalling the basic geometric features of the proposed antenna, our initial realization has $\tau = 0.975$, $\tau_{oa} = \tau_a = 20^\circ$, and $\tau_b = 0.67^\circ$, which create a total volume of 1.906 cm^3 . For its discretization, an FDTD mesh of $407 \times 407 \times 359 \approx 59.47$ million cells (around 3.52 GB RAM and 11 hours of CPU time) is generated. Since the new PLPAs must exhibit a satisfactory performance for diverse arm geometries, our investigation focuses, first, on the impact of their teeth thickness t_n variation as a percentage of distance s_n . So retaining constant the rest of the design parameters. Figure 3 presents a set of directivity and half-power beamwidth angle (HPBA) comparisons. As derived, t_n variations do not considerably affect the main PLPA radiation features, especially when thicker elements are employed. This deduction is also confirmed by the radiation patterns of Fig. 4, computed for two different φ angles at the limits of the desired frequency range. Bearing in mind the prior aspects, t_n is set equal to the 20 % of s_n , for the remainder of this study, which is proven a very practical choice. Notice that HPBA is similar over the two ($\varphi = 0^\circ, 90^\circ$) perpendicular planes, a fact which certifies the fulfillment of the important condition for a circular 3-dB contour. Also a closer inspection of Figs. 3 and 4 reveals that the frequency spectrum for an efficient operation of the novel PLPA extends approximately from 15 GHz to 110 GHz; an important profit, which amply meets the standards of modern UWB applications. Indeed, in this practically 100 GHz frequency range, no main lobe deviations or directivity reductions have been observed. Moreover, Fig. 5 illustrates the surface current density on one arm of the PLPA, with its maximum values detected at the larger teeth for higher frequencies.



(a)

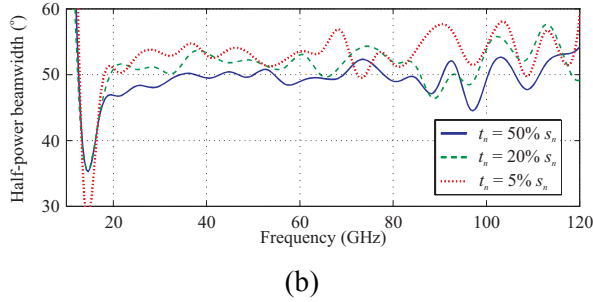


Fig. 3. Performance comparison of several PLPAs for different t_n values as a percentage of s_n ; (a) directivity and (b) half-power beamwidth angle.

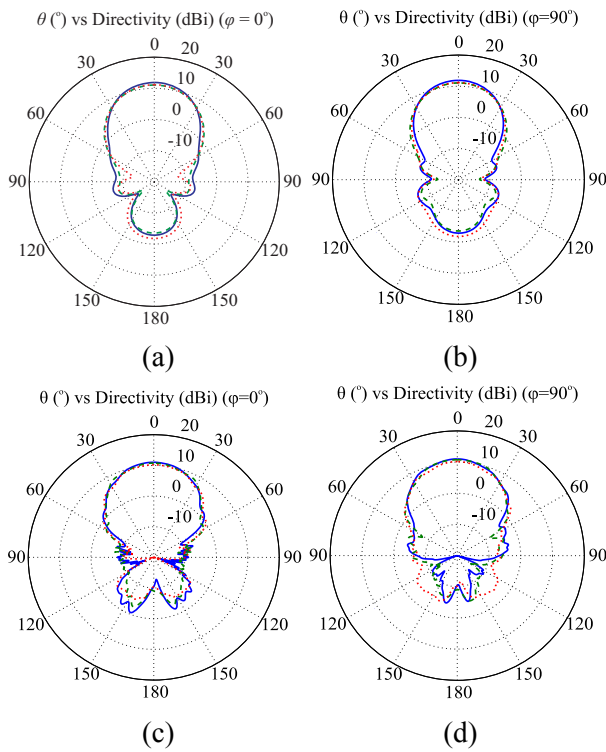


Fig. 4. Radiation patterns of various PLPAs with $t_n = 0.5s_n$ (blue continuous line), $t_n = 0.2s_n$ (green dashed line), and $t_n = 0.05s_n$ (red dotted line) at (a), (b) $f= 20$ GHz and (c), (d) $f= 100$ GHz.

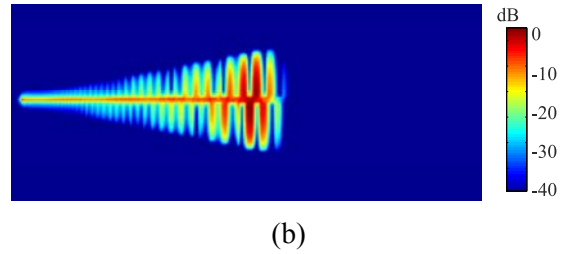
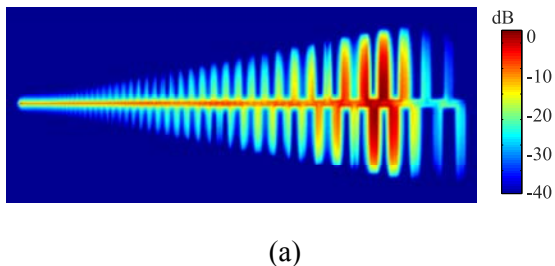


Fig. 5. Surface current density of the proposed PLPA at (a) $f= 20$ GHz and (b) $f= 40$ GHz.

Proceeding with our analysis, we now concentrate on the factors that can more prominently influence the antenna’s volume, namely angles τ_{oa} and τ_a , which, as already explained, must be equal. To this objective, a parametric study pertaining to the variations of these angles is conducted, with the rest of the PLPA features set to their initial values. In this context, Fig. 6 shows the results of our simulations, compared with the performance of the already modeled initial device, i.e., $\tau_{oa} = \tau_a = 20^\circ$. Specifically, keeping all the FDTD implementation details of subsection II. B the same, for the case of $\tau_{oa} = \tau_a = 25^\circ$, we build a grid with $407 \times 407 \times 289 \approx 48.87$ million cells (about 2.83 GB RAM and 8.85 hours of CPU time), whereas for $\tau_{oa} = \tau_a = 30^\circ$ a mesh of $407 \times 407 \times 243 \approx 40.25$ million cells (about 2.36 GB RAM and 7.44 hours of CPU time). It occurs that as τ_a increases, the directivity is significantly reduced, while HPBA is slightly augmented. Also, the radiation patterns of Fig. 7 indicate that larger angles introduce amplified side lobes, with regard to the main one. However, the most advantageous asset of this optimization process is the notably decreased overall volume of the resulting device and the required FDTD lattice, as well. In fact, the PLPA total volume minimizes with the increment of τ_{oa} , as deduced by equation (1). Explicitly, this reduction is about 21.1 % for $\tau_{oa} = \tau_a = 25^\circ$ and around 35.4 % for $\tau_{oa} = \tau_a = 30^\circ$; a fact also deduced by the corresponding grid sizes. Consequently, it is evident that the above process can lead to very proficient and compact PLPAs for UWB designs.

In order to validate the advantages of the improved PLPAs, a set of prototypes has been carefully fabricated. In particular, two different antennas have been constructed with respect to angle τ_a i.e., a triangular-toothed PLPA with $\tau_a = 25^\circ$ and a Eu-

clidean-toothed PLPA with $\tau_a = 30^\circ$, as indicatively illustrated in Fig. 8, along with the measurement setup. So, Fig. 9 provides the comparisons between measured data and simulated outcomes concerning the isolation of the two vertical polarizations for each one of the two fabricated PLPAs. As deduced, their agreement is very satisfactory, thus proving the significant contribution of the proposed technique in the performance of the specific radiators.

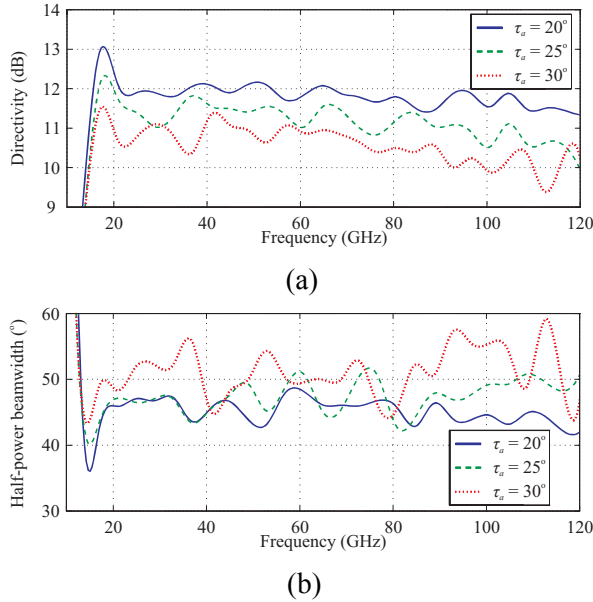


Fig. 6. Performance comparison of several PLPAs for different τ_a values, (a) directivity and (b) half-power beamwidth angle.

III. THE VOLUME-OPTIMIZED MEANDER-TOOTHED PLPA

A. Development of the design procedure

A meander line is a self-avoiding closed curve, which can intersect with a straight line at a finite number of points. The principal aim of its use at the teeth of the new PLPAs is the substantial overall size reduction it attains, as it leads to a smaller single tooth with the same electrical length. A typical 2nd-order meander curve is depicted in Fig. 10 (a) along with its basic design parameters applied to its entire length. To evaluate the desired electrical length l_{en} , the approximation of

$$l_{en} = l_n + 2c_n = 2a_n + b_n + 2c_n, \quad (6)$$

with the restriction $b_n > 2t_n$, is deemed a viable selection to avoid overlapping. Nevertheless, when the meander elements are placed together to form

the antenna arm, some additional conventions need to be determined. Firstly, the distance w_n between two consecutive same-sided elements is finite and therefore the value of c_n should have an upper limit. Exploiting the pattern of the elements, Fig. 10 (c) shows that w_n can be precisely expressed as

$$w_n = s_n + s_{n-1} = s_n (1 + \tau^{-1}). \quad (7)$$

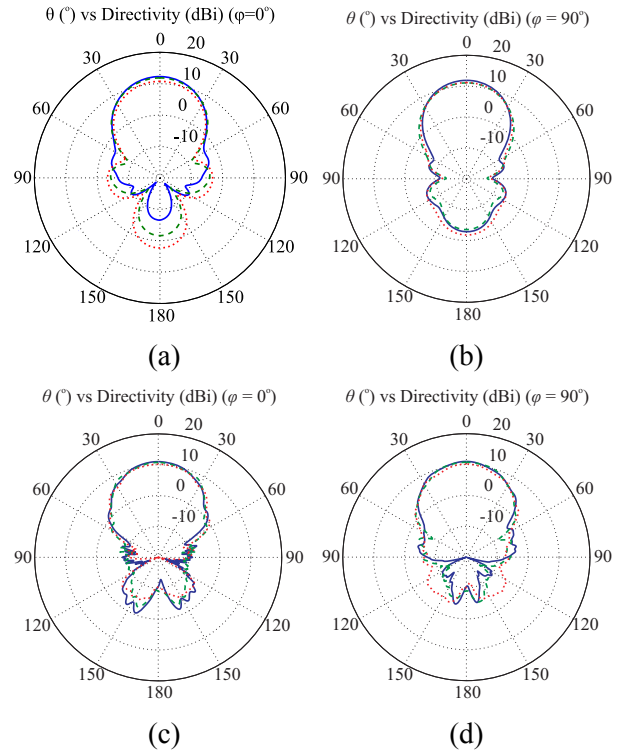


Fig. 7. Radiation patterns of different PLPAs with $\tau_a = 20^\circ$ (blue continuous line), $\tau_a = 25^\circ$ (green dashed line), and $\tau_a = 30^\circ$ (red dotted line) at (a), (b) $f = 20$ GHz and (c), (d) $f = 100$ GHz.

So, the restriction for c_n is imposed by means of,

$$c_n < w_n - t_n. \quad (8)$$

An effective way to increase the available space stems from the reduction of scale factor τ , as derived by equations (6) and (7); an issue that will be elaborately examined in the following paragraphs for large τ values. Furthermore, the presence of the central boom introduces a lower limit for a_n in order to evade possible element overlapping, as displayed in Fig. 10 (b). This constraint is satisfied via

$$a_1 > l_{\max} \frac{\tan(\tau_b / 2)}{\tan(\tau_{oa} / 2)}, \quad (9)$$

regarding the first tooth only. Observe however that the fulfillment of equation (9) is, also, applicable to the rest of the teeth, due to the scaling properties of LPAs. Hence, considering the prior analysis, meander elements are, herein, formed through the design of Fig. 10 (a) to enhance the competence of our method.

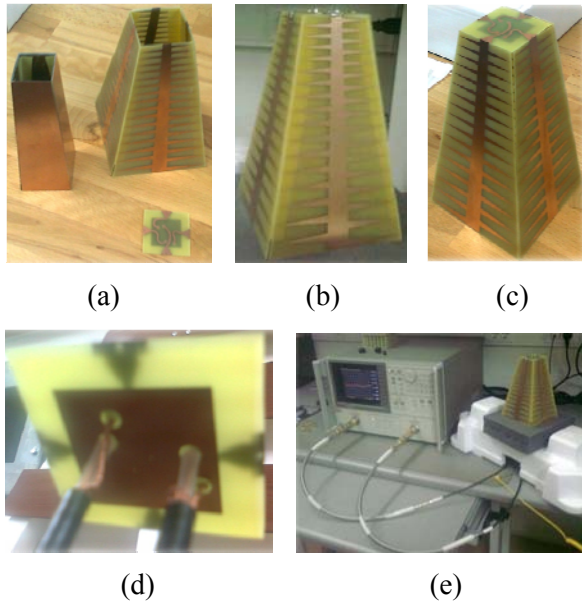


Fig. 8. The volume-confined PLPAs; (a) parts: four-arm radiator, conductive shield, and planar feeding circuit, (b), (c) views of the fabricated prototypes, (d) transmission line cables of the feeding system (internal side), and (e) measurement setup.

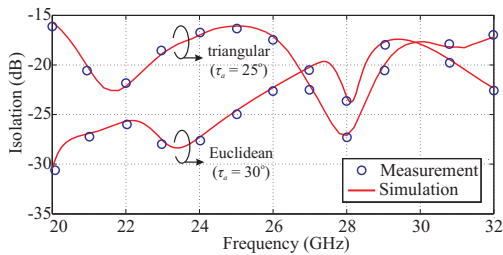


Fig. 9. Isolation of the fabricated triangular- and Euclidean-toothed volume-confined PLPAs.

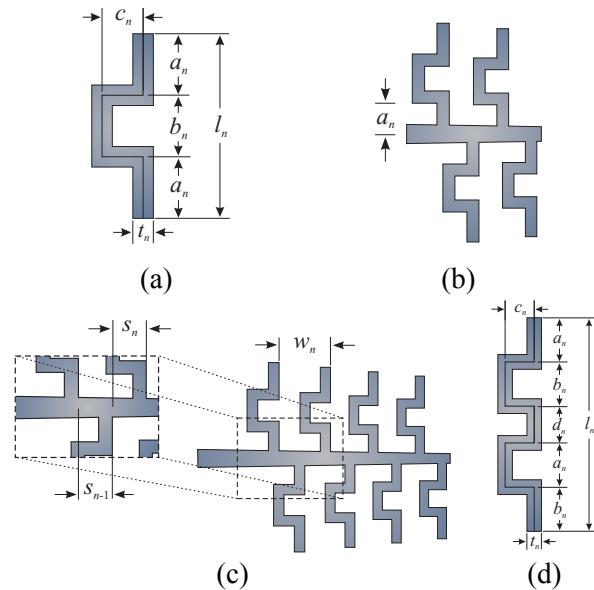


Fig. 10. (a) A 2nd-order meander element with (b), (c) its main design parameters, and (d) a 3rd-order meander element.

B. Applications and numerical validation

Next and after the specification of its upper limit through equation (8), let us concentrate on the effect of c_n variations. To this goal, three meander-toothed radiators of the proposed PLPA family are designed in which c_n is equal to the 50 %, 60 %, and 70 % of the maximum possible $w_n - t_n$ value. Thus, the grid consists of, (a) $323 \times 323 \times 359 \approx 37.45$ million cells (about 2.21 GB RAM and 6.92 hours of CPU time), for $c_n = 0.5 (w_n - t_n)_{\max}$, (b) $310 \times 310 \times 359 \approx 34.5$ million cells (about 2.04 GB RAM and 6.38 hours of CPU time) for $c_n = 0.6 (w_n - t_n)_{\max}$, and (c) $220 \times 220 \times 359 \approx 17.3$ million cells (about 1.03 GB RAM and 3.1 hours of CPU time) for $c_n = 0.7 (w_n - t_n)_{\max}$. Note that the rest of the FDTD details are those described in subsection II. B. Furthermore, the thickness of the teeth is set to $t_n = 0.2s_n$, whereas $a_n = b_n$ are evaluated using equation (6). The prior setups offer a notable decrease of the total volume and the FDTD lattice in comparison with those of the initial antenna, i.e., 41 %, 47.3 %, and 53 %, respectively. In order to realize this decrease, Fig. 11 presents the geometry of a Euclidean-toothed and a meander-toothed PLPA with the same properties. Obviously, the volume of the latter is proven to be much smaller and sufficiently more compact. On the other hand, directivity and HPBA results are shown in Fig. 12, while the corresponding radiation patterns

are given in Fig. 13. Note that all volume-optimized antennas exhibit a very satisfactory performance in the preselected 20 GHz to 80 GHz spectrum. Nonetheless and as anticipated, these radiation characteristics start to deteriorate at higher frequencies, mainly due to the proximity of consecutive elements operating at the specific frequency region. This is attributed to the more prominent influence of parasitic capacitances, which change the electrical length of the elements and thus affects the device's behavior.

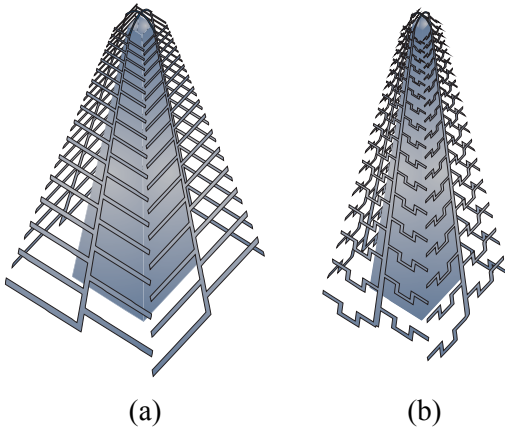
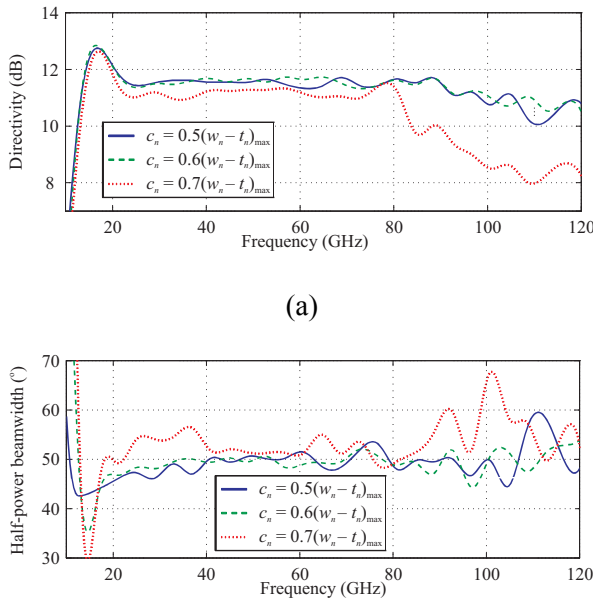


Fig. 11. Geometry of (a) the Euclidean-element and (b) the proposed meander-element PLPA.



(b)

Fig. 12. Comparison between different meander-toothed PLPAs versus c_n , expressed as a percentage of the maximum $w_n - t_n$ value, (a) directivity and (b) half-power beamwidth angle.

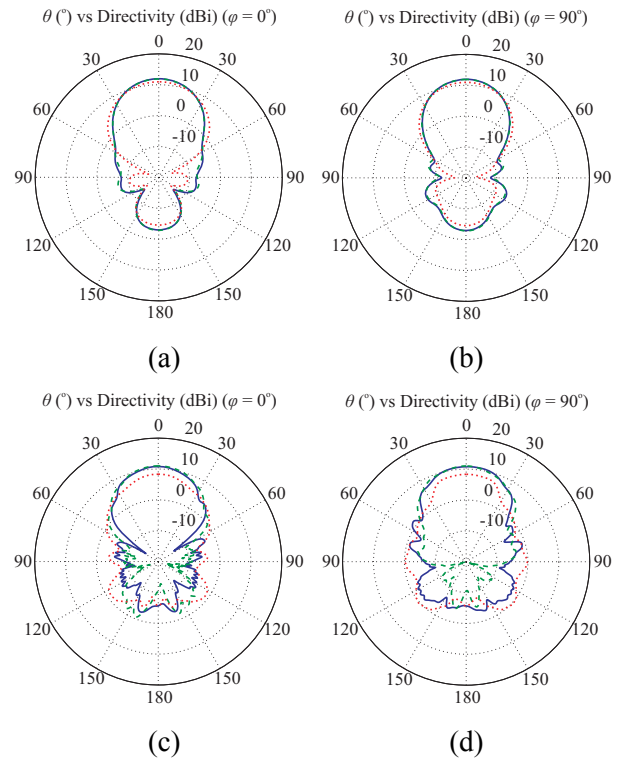
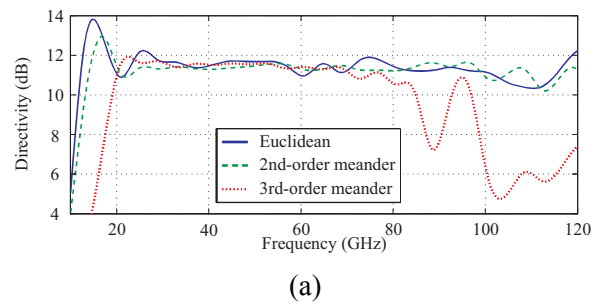


Fig. 13. Radiation patterns of diverse PLPAs with $c_n = 0.5 (w_n - t_n)$ (blue continuous line), $c_n = 0.6 (w_n - t_n)$ (green dashed line), and $c_n = 0.7 (w_n - t_n)$ (red dotted line) at (a), (b) $f = 20$ GHz, and (c), (d) $f = 100$ GHz.



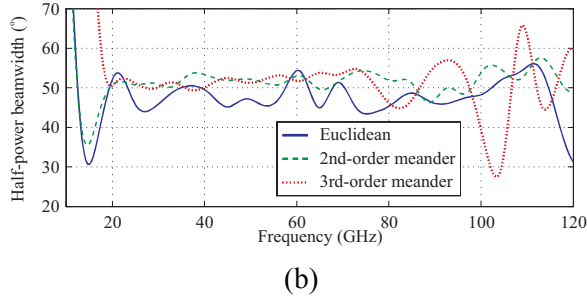


Fig. 14. Comparison between various PLPAs with different elements; (a) directivity and (b) half-power beamwidth.

The last PLPA arrangement involves the incorporation of the 3rd-order meander element of Fig. 10 (d). Its design is conducted by considering that

$$l_{en} = l_n + 4c_n = 2a_n + 2b_n + d_n + 4c_n. \quad (10)$$

The rest of the constraints are identical to those introduced by equations (8) and (9) for the 2nd-order meander teeth. For our investigation, we compare a Euclidean-toothed PLPA ($\tau = 0.975$, $\tau_b = 0.67^\circ$, $\tau_{oa} = 20^\circ$) with two meander-toothed PLPAs based on 2nd- and 3rd-order elements. All τ , τ_b , and τ_{oa} values remain the same, except for $c_n = 0.6$ ($w_n - t_n$) and $t_n = 0.25s_n$. Moreover, $a_n = b_n$ are computed using equation (5) for the 2nd-order meanders, whereas $a_n = b_n = d_n$ are derived using equation (10) for the 3rd-order case. It should be emphasized that the total volume reduction reaches the impressive level of 50 % for the second and 81.7 % for the third configuration.

To verify the proposed structures, numerical results, acquired by our FDTD simulations, are summarized in Figs. 14 and 15. Therefore, using the FDTD set-up of the previous example for the 2nd-order case, we discretize the 3rd-order meander element radiator by means of a $138 \times 138 \times 359 \approx 6.83$ million-cell grid (around 0.4 GB RAM and 1.26 hours of CPU time). Again, the properties of the meander-element PLPAs are very sufficient in the prefixed region of 20 GHz to 80 GHz, so indicating the efficiency of the volume-confinement concept. At high frequency regions, though, the operation of the 3rd-order meander-toothed device degrades owing to the presence of parasitic capacitances, which reveals a trade-off between compactness and high directivity beamwidth for these antennas. Nonetheless, the behavior of its 2nd-order counterpart resembles that of the conventional PLPA achieving a better compression ratio in UWB applications. Finally, the surface current distributions of

the two meander-toothed PLPAs are visualized in Fig. 16, to indicate the smoothness in the propagation of the electromagnetic field energy. As a consequence and based on the aforementioned promising outcomes, it is deduced that the proposed miniaturization technique can be productively employed in several contemporary high-end communication appliances with a noteworthy performance.

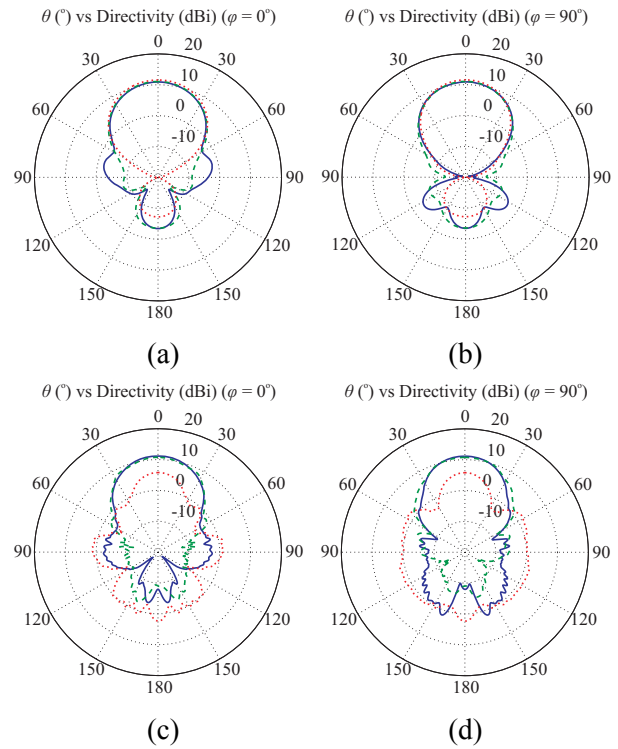
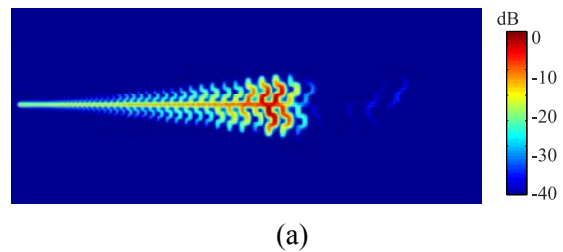
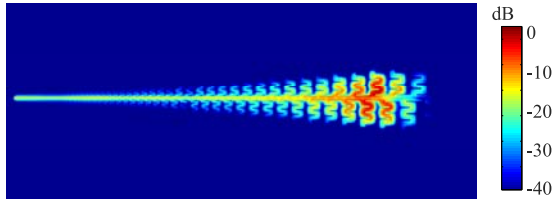


Fig. 15. Radiation patterns of diverse PLPAs with Euclidean (blue continuous line), 2nd-order meander (green dashed line), and 3rd-order meander (red dotted line) elements at (a), (b) $f = 20$ GHz, and (c), (d) $f = 100$ GHz.





(b)

Fig. 16. Surface current density of two volume-optimized meander-toothed PLPAs; (a) 2nd-order at $f = 40$ GHz and (b) 3rd-order at $f = 20$ GHz.

IV. CONCLUSION

The optimal design and comprehensive characterization of a general PLPA class for modern UWB implementations have been presented in this paper. Focusing on the critical issue of overall volume reduction and the strict requirement for compact dimensions, a new meander-toothed configuration, occupying significantly less space than the conventional Euclidean-toothed structure, has been introduced. Essentially, the primary concept lies on the determination of certain constraints during the design of the meander elements. Aside from being fabricated and measured, the efficient devices have been successfully verified by means of a 3-D FDTD method. Extensive numerical simulations, addressing directivity, half-power beamwidth, and other instructive radiation characteristics, confirm that the specific PLPAs can suitably satisfy the UWB application standards, while the decreased volume does not influence their useful operational behavior.

ACKNOWLEDGMENT

This research has been co-financed by the EU (European Social Fund – ESF) and Greek national funds through the Operational Program “Education and Lifelong Learning” of the National Strategic Reference Framework (NSRF) – Research Funding Program: ARISTEIA I. Investing in knowledge society through the European Social Fund.

REFERENCES

- [1] D. Anagnostou, J. Papapolymerou, M. Tentzeris, and C. Christodoulou, “A printed log-periodic Koch-dipole array (LPKDA),” *IEEE Antennas Wireless Propag. Lett.*, vol. 7, pp. 456-460, 2008.
- [2] C. de J. van Coevorden, A. Bretones, M. Pantoja, S. García, A. Monorchio, and R. Martín, “A new implementation of the hybrid Taguchi GA: Application to the design of a miniaturized log-periodic thin-wire antenna,” *ACES Journal*, vol. 24, no. 1, pp. 21-31, 2009.
- [3] S. Kurokawa, M. Hirose, and K. Komiyama, “Measurement and uncertainty analysis of free-space antenna factors of log-periodic antenna using time-domain techniques,” *IEEE Trans. Instrum. Meas.*, vol. 58, no. 4, pp. 1120-1125, 2009.
- [4] J. Yang and P. Kildal, “Optimization of reflection coefficient of large log-periodic array by computing only a small part of it,” *IEEE Trans. Antennas Propag.*, vol. 59, no. 6, pp. 1790-1797, 2011.
- [5] H. Nouri, J. Nourinia, and C. Ghobadi, “Multi-band printed dipole antenna with log-periodic toothed structure for WLAN/WiMAX applications,” *Microw. Opt. Technol. Lett.*, vol. 53, no. 3, pp. 536-539, 2011.
- [6] J. Yeo and J.-I. Lee, “Planar log-periodic bow-tie dipole array antenna with reduced size and enhanced front-back ratio,” *Microw. Opt. Technol. Lett.*, vol. 54, no. 6, pp. 1435-1441, 2012.
- [7] O. Ergül and L. Gürel, “Non-planar trapezoidal tooth log-periodic antennas: design and electromagnetic modeling,” *Radio Sci.*, vol. 40, no. RS5010, pp. 1-14, 2005.
- [8] G. Engargiola and W. Welch, “Log-periodic antenna,” US Patent 6.677.913 B2, 2004.
- [9] N. Haridas, A. El-Rayis, A. Erdogan, and T. Arslan, “Multi-frequency antenna design for space-based reconfigurable satellite sensor node,” *Proc. 2nd NASA/ESA Conf. Adaptive Hardware Systems*, pp. 1-6, 2007.
- [10] S. Kim, S. Lee, and Y. Kim, “Multi-band monopole antenna using meander structure for handheld terminals,” *Electron. Lett.*, vol. 44, no. 5, pp. 331-332, 2008.
- [11] P. Izdebski, H. Rajagopalan, and Y. Rahmat-Samii, “Conformal ingestible capsule: A novel chandelier meandered design,” *IEEE Trans. Antennas Propag.*, vol. 57, no. 4, pp. 900-909, 2009.
- [12] Y. Zhang, N. Nikolova, and M. Bakr, “Input impedance sensitivity analysis of patch antenna with discrete perturbations on method-of-moment grids,” *ACES Journal*, vol. 25, no. 10, pp. 867-876, 2010.
- [13] B. Devireddy, A. Yu, F. Yang, and A. Elsherbeni, “Gain and bandwidth limitations of reflectarrays,” *ACES Journal*, vol. 26, no. 2, pp. 170-178, 2011.
- [14] W. -T. Hsieh and J. -F. Kiang, “Small broadband antenna composed of dual-meander folded loop and disk-loaded monopole,” *IEEE Trans. Antennas Propag.*, vol. 59, no. 5, pp. 1716-1720, 2011.
- [15] M. Mohammadirad, N. Komjani, A. Sebak, and M. Chaharmir, “A broadband reflectarray antenna using the triangular array configuration,” *ACES Journal*, vol. 26, no. 8, pp. 640-650, 2011.

- [16] Y. Watanabe, K. Watanabe, and H. Igarashi, "Optimization of meander line antenna considering coupling between nonlinear circuit and electromagnetic waves for UHF-band RFID," *IEEE Trans. Magn.*, vol. 47, no. 5, pp. 1506-1509, 2011.
- [17] M. Zoppi, C. Dedeban, C. Pichot, S. Selleri, and G. Pelosi, "Optimal location of multi-antenna systems - Influence of noise-corrupted data," *ACES Journal*, vol. 27, no. 2, pp. 198-205, 2012.
- [18] W. Weng, "Optimal design of an ultra-wide-band antenna with the irregular shape on radiator using particle swarm optimization," *ACES Journal*, vol. 27, no. 5, pp. 427-434, 2012.
- [19] J. -P. Berenger, "A perfectly matched layer for the absorption of electromagnetic waves," *J. Comp. Phys.*, vol. 114, pp. 185-200, 1994.
- [20] A. Taflove and S. Hagness, *Computational Electrodynamics: The Finite-Difference Time-Domain Method*, Artech House, 2005.
- [21] Y. Zhang, A. Kishk, A. Yakovlev, and A. Glisson, "FDTD analysis of a probe-fed dielectric resonator antenna in rectangular waveguide," *ACES Journal*, vol. 21, no. 1, pp. 37-44, 2006.
- [22] M. Hadi, "Wide-angle absorbing boundary conditions for low and high-order FDTD algorithms," *ACES Journal*, vol. 24, no. 1, pp. 9-15, 2009.



Stamatios A. Amanatiadis received the Diploma degree in Electrical and Computer Engineering from the Aristotle University of Thessaloniki, Greece, in 2010, where he is currently pursuing his Ph.D. degree. His research focuses on modern antenna design, analysis of graphene structures, and computational electromagnetics.



Antonios X. Lalas received the Diploma and the Ph.D. degrees in Electrical and Computer Engineering from the Aristotle University of Thessaloniki, Greece, in 2006 and 2011, respectively. His research interests include numerical methods, antenna and MEMS modeling, with an emphasis on EBGs and metamaterials.



Nikolaos V. Kantartzis received the Diploma and Ph.D. degrees from the Department of Electrical

and Computer Engineering, Aristotle University of Thessaloniki, Greece, in 1994 and 1999, respectively. In 2001, he joined the same department, as a Postdoctoral Research Fellow, where, currently, he serves as an Assistant Professor. He has authored/co-authored 3 books, more than 70 refereed journal and over 90 conference papers. His main research interests focus on EMC modeling, computational electromagnetics, antenna analysis, higher-order time- and frequency-domain methods, metamaterials, and advanced microwave structures. Dr. Kantartzis is a member of diverse societies and associations.

Theodoros D. Tsiboukis received the Diploma degree in Electrical and Mechanical Engineering from the National Technical University of Athens, Athens,



Greece, in 1971, and the Doctor Eng. Degree from the Aristotle University of Thessaloniki (AUTH), Greece, in 1981. From 1981 to 1982, he was with the Electrical Engineering Department, University of Southampton, U.K., as a Senior Research Fellow. Since 1982, he has been with the Department of Electrical and Computer Engineering, AUTH, where he is currently a Professor. He has served in numerous administrative posts and as a chairman of many conference committees. He is the author of 8 books and over 280 refereed journal and conference papers. His research areas, primarily, include frequency- and time-domain computational electromagnetics, metamaterials, graphene, and EMC problems. Prof. Tsiboukis is a member of various societies, associations, and institutions, and has received several awards and distinctions.